G. Gori, G. Parma, M. Zocca, A. Guardone
Local Solution to the Unsteady Stefan Problem for In-Flight Ice Accretion Modeling
Journal of Aircraft, Vol. 55, N. 1, 2018, p. 251-262
doi:10.2514/1.C034412

Local solution to the unsteady Stefan problem for in-flight ice accretion modeling

Giulio Gori[1], Gianluca Parma[2], Marta Zocca[3], Alberto Guardone[4]
Politecnico di Milano, Department of Aerospace Science and Technology,

Via La Masa 34, 20156 Milano, Italy

A new model for in-flight ice accretion is presented for both rime and glaze conditions. The model is based on the local, exact solution of the unsteady Stefan problem for the temperature profiles within the ice layer in glaze conditions. The new model moves from Myers' formulation and it includes an unsteady description of the heat diffusion problem within the ice layer. Moreover, the local value of the air temperature outside the boundary layer is used to compute convective heat fluxes, in place of the constant free-stream temperature value considered in Myers model. A source term is introduced to take into account mass transfer at the boundary separating rime and glaze regions. The model was implemented in the ice accretion software PoliMIce to perform numerical simulations of in-flight ice accretion over two-dimensional airfoils in both rime and glaze ice regimes. The open-source CFD software OpenFOAM was used to compute the aerodynamic flow field and to reconstruct water droplet trajectories. Numerical results suggest that the modifications introduced with respect to the original Myers model improve significantly the accuracy of the predicted ice shapes for the considered test cases. The introduction of the local value of air temperature was found to be essential for the formation of the well-known two-horn ice shape, due to the occurrence of a local glaze to rime transition. The diverse contributions to the heat fluxes are discussed for both the proposed and the Myers models.

---

[1] Ph.D. Candidate, Department of Aerospace Science and Technology, Politecnico di Milano
[2] Research Assistant, Department of Aerospace Science and Technology, Politecnico di Milano.
[3] Ph.D. Candidate, Department of Aerospace Science and Technology, Politecnico di Milano
[4] Full Professor, Department of Aerospace Science and Technology, Politecnico di Milano, AIAA Member, Corresponding author

Nomenclature

t = Time, s

B = Ice layer thickness, m

h = Liquid water film thickness, m

z_1 = Vertical coordinate within the ice layer originating from the surface of the body ($0 < z_1 < B$), m

z_2 = Vertical coordinate within the liquid water layer originating from the ice-water interface ($0 < z_2 < h$), m

A = Area of the elementary superficial domain, m^2

T_f = Freezing temperature (273.15 K for water), K

T_w = Wall temperature (also referred to as substrate), K

$T(z_1)$ = Temperature distribution within the ice layer, K

$\vartheta(z_2)$ = Temperature distribution within the liquid water layer, K

β = Collection efficiency

α = Angle of attack, deg

V_∞ = Free-stream velocity, m/s

T_∞ = Free-stream temperature, K

P_∞ = Free-stream static pressure, Pa

K = Thermal conductivity, W/mK

ρ = Density, $\mathrm{kg/m}^3$

C_P = Specific heat at constant pressure, J/kgK

$\dot{Q}$ = Heat flux, $\mathrm{W/m}^2$

$\dot{Q}_\mathrm{l}$ = Heat flux due to phase change, $\mathrm{W/m}^2$

$\dot{Q}_\mathrm{c}$ = Heat flux due to convection, $\mathrm{W/m}^2$

$\dot{Q}_\mathrm{e}$ = Heat flux due to evaporation, $\mathrm{W/m}^2$

$\dot{Q}_\mathrm{s}$ = Heat flux due to sublimation, $\mathrm{W/m}^2$

$\dot{Q}_\mathrm{d}$ = Heat flux due to droplet latent heat, $\mathrm{W/m}^2$

$\dot{Q}_\mathrm{k}$ = Heat flux due to droplet kinetic energy, $\mathrm{W/m}^2$

$\dot{Q}_\mathrm{a}$ = Heat flux due to air friction, $\mathrm{W/m}^2$

$\dot{Q}_\mathrm{top}$ = Heat flux exchanged between the phase changing interface and water (or air), $\mathrm{W/m}^2$

$\dot{Q}_\mathrm{bottom}$ = Heat flux exchanged between the phase changing interface and ice, $\mathrm{W/m}^2$

$\dot{m}$ = Mass flux, kg/s

$\dot{m}_{\mathrm{fr}}$ = Mass flux due to phase change, kg/s

$\dot{m}_{\mathrm{h}}$ = Mass flux due to water film thickness change, kg/s

$\dot{m}_{\mathrm{in}}$ = Mass flux due to liquid water incoming from neighbouring cells, kg/s

$\dot{m}_{\mathrm{out}}$ = Mass flux due to liquid water leaving to neighbouring cells, kg/s

$\dot{m}_{\mathrm{s}}$ = Mass flux due to sublimation, kg/s

L = Latent heat, J/Kg

L_{f} = Latent heat of fusion, J/Kg

L_{s} = Latent heat of sublimation, J/Kg

L_{e} = Latent heat of evaporation, J/Kg

Subscripts

i = Ice

w = Liquid water

I. Introduction

Protection from atmospheric hazards is one of the most demanding challenges in the design of a new aircraft. During its lifespan, an aircraft experiences a wide variety of environmental conditions, which often change abruptly during normal operation. For example, only a short period of time elapses from passenger boarding to the far-below-freezing conditions at cruising altitude. Manufacturers must guarantee safety against all possible atmospheric hazards a flying machine may encounter—unexpected wind gusts, rain, snow and ice, among others.

Exposure to clouds composed by super-cooled droplets or to precipitations such as freezing rain or drizzle possibly leads to the accumulation of ice on critical components of the aircraft [1]. Super-cooled droplets hold in an unstable equilibrium state which is perturbed by the impact against the aircraft surface. The impact triggers water to freeze [2] and it possibly results in the formation of an ice layer which modifies the shape of the airfoil sections. As a result, aerodynamic performances are significantly compromised: maximum lift drops, stall angle reduces and parasite drag increases [3]. Ice accretion over engine nacelle alters the airflow in the inlet manifold, whereas the ice accumulating

on rotating devices—such as for example compressor blades, helicopter rotors or propellers—possibly results in ice shedding and aerodynamic and structural load unbalancing [4]. Moreover, localized ice structures accumulating on external sensors may cause misleading information to be conveyed to the pilot; ice accreting on the inner mechanisms of control surfaces may lead to mechanical lock of the control surfaces themselves. As a result, aircraft stability and control—and hence passengers safety—are severely compromised [5].

The interest towards ice accretion is not only limited to the aerospace industry, but it is also relevant in nautical and civil applications. A considerable research effort is being devoted to the design of power generation and distribution plants located in alpine environments. Ice build-up reduces the efficiency of wind turbine blades, thus affecting energy production. Moreover, power cables and antennas are slender structures which can get damaged by the overload introduced by the accreted ice or due to the activation of destructive aeroelastic modes. [6, 7].

The development of effective ice protection systems, which allows to improve safety standards and, at the same time, reduce operational costs and the environmental impact, calls for a deeper knowledge of the ice accretion process and for an accurate prediction of the related performance degradation mechanism. Reliable investigation tools may help researchers and engineers understanding ice accretion.

In this report, flight and wind tunnel tests and numerical simulations are complementary approaches to the study of ice accretion; each of them is applied to a different extent in each step of the design process.

From the numerical standpoint, a number of icing prediction codes (see e.g. Refs. [8–15]) were developed to complement the experimental activity during the design and certification of new aircraft. Comparison of numerical results with experimental ice shapes allows to test existing models and to fine-tune new ones.

The physical description of ice formation usually discerns between two different accretion mechanisms which are relevant to aerospace applications and whose occurrence depends on environmental conditions. These two processes lead to ice build-ups of different nature, which are commonly identified as either *rime* ice or *glaze* ice [16–18], respectively. Droplets which freeze immediately at

impact against the wing surface originate a layer of so-called rime ice. When, instead, the impinging droplets do not freeze instantaneously, a thin liquid layer lies on top of a previously accreted ice layer. This thin film of unfrozen water, which either flows downstream or sheds off the body under the action of aerodynamic and gravitational forces results in glaze ice formations. Therefore a mathematical model aimed at predicting ice accretion in a wide range of operating conditions must be able to deal with both rime and glaze conditions. This ability is usually achieved by defining two different accretion laws—one for the rime and one for the glaze regime—and a reliable criterion to select the most suitable.

Messinger's model [16] and its extension [17] are examples of current state-of-the-art icing models. Notwithstanding the many simplifying hypotheses introduced, these models are capable of predicting acceptable ice shapes within certain ranges of environmental conditions. As suggested by Myers[17], one of the major drawbacks of Messinger model is that it usually underestimates the ice layer thickness, since it neglects heat conduction within the ice layer. In order to correct this deficiency, Myers [17] proposed an accretion model based on the solution of a Stefan problem—namely, a set of four partial differential equations describing the evolution of a single-component two-phase system—within elementary control volumes. Among the hypotheses underlying the model (discussed here in section II C), the most critical ones are the assumption that the time scale governing heat diffusion is much smaller than that of ice accretion, which in turn leads to a steady description of the heat diffusion problem. As a consequence, the ice substrate is assumed to be isothermal. Unfortunately, the linear temperature profile in the ice layer resulting from the model equations is not consistent with the assumption of an isothermal substrate, which instead force an infinite derivative of the temperature profile at the wall.

In the present work, a new ice accretion model aimed at investigating the aforementioned inconsistencies of Myers model is proposed. Moving from Myers model, the heat diffusion dynamics is taken into account and the hypothesis that the time scale of heat diffusion is smaller than the time scale of ice accretion is released. The heat diffusion within the ice layer in glaze conditions is thus described through the analytic solution of the Fourier heat equation. The novel model also includes a modification of the terms related to the heat exchanged by convection with the external airflow:

differently from Myers model, the local value of the airflow temperature due to air compressibility effects is accounted for. The new model is implemented in the PoliMIce software [15], an ice accretion simulation framework developed at the Department of Aerospace Science and Technology of Politecnico di Milano. Its highly modular structure provides a flexible interface among different CFD and ice-accretion models [15, 19]. In the PoliMIce suite, both the original Myers model [17] and the novel one are implemented. Results obtained by applying these two models are compared to experimental ice shapes, in order to assess the modifications to the original model.

In the following section, a brief introduction to the existing icing models and the detailed description of the proposed ice accretion model are provided. Differences with respect to the original Myers model are discussed. In Sec. III the PoliMIce suite and the ice accretion calculation procedure are presented. Numerical results obtained by applying these two icing models are also reported and discussed. Finally, Sec. IV provides concluding remarks.

II. Icing models

Starting from the fundamental formulations proposed by F. Neumann, B.P. Clapeyron and G. Lamé, among others, J. Stefan gave a first mathematical description of the water-ice two-phase problem in 1891 [20], in connection with ice formation in the polar sea. Moving from these early works, the so-called Stefan problem was then generalized to describe other physical systems where phase change can possibly occur, such as e.g. solid/liquid metal interfaces in melting processes.

In 1953, Messinger [16] developed the first formulation of the Stefan problem for aeronautical applications. In 2001, Myers [17] presented an extension to the Messinger icing model. Starting from Messinger's work, the model formulated by Myers introduced a more accurate description of the transition from rime to glaze ice regime. Differently from Messinger model, in which the substrate is assumed to be insulated, Myers added a description of heat diffusion through the ice and the water layers, in order to take into account the heat transfer at the aircraft surface [17].

In the present work, a novel icing model based on the exact solution of the Stefan problem is presented. While the formulation describing the rime ice regime does not differ substantially from the one proposed by Myers, the formulation related to the glaze ice regime includes an unsteady

Table 2 Typical values of the parameters used to define the ice accretion problem.

Density	ρ_{w}	1000 $[Kg/m^3]$	$\rho_{\mathrm{i_{rime}}}$	880 $[Kg/m^3]$
	$\rho_{i_{\mathrm{glaze}}}$	917 $[Kg/m^3]$		
Latent heat	L_{S}	$2.83 \cdot 10^3$ $[J/Kg]$	L_{F}	$3.344 \cdot 10^5$ $[J/Kg]$
	L_{E}	$2.26 \cdot 10^6$ $[J/Kg]$		
Specific heat	$C_{\mathrm{P_w}}$	4218 $[J/KgK]$	$C_{\mathrm{P_i}}$	2050 $[J/KgK]$
Thermal conductivity	K_{w}	0.571 $[W/mK]$	K_{i}	2.18 $[W/mK]$

treatment of the heat diffusion problem within the ice layer. Moreover, the local value of the airflow temperature resulting from the CFD simulation is used to calculate the heat exchanged by convection at the water-air interface, in place of the free-stream static temperature. In the next sections, the Stefan problem is briefly recalled (Sec. II A) and the Myers model is discussed (Sec. II B). In Section II C, the new icing model is presented and differences with respect to Myers model are pointed out and commented. The reader is referred to the Nomenclature section for the description of the diverse parameters and physical quantities introduced in the following exposition and to Ref. [17] for their complete mathematical definitions.

A. Stefan problem

The Stefan problem is a set of four Partial Differential Equations (PDEs) describing the evolution of a single-component two-phase system. It reads

$$\begin{cases} \dfrac{\partial T}{\partial t} = \alpha_{\mathrm{i}} \dfrac{\partial^2 T}{\partial z_1^2} \\ \dfrac{\partial \vartheta}{\partial t} = \alpha_{\mathrm{w}} \dfrac{\partial^2 \vartheta}{\partial z_2^2} \\ \Delta \dot{Q} = \dot{Q}_{\mathrm{top}} + \dot{Q}_{\mathrm{bottom}} \\ \dot{m}_{\mathrm{fr}} + \dot{m}_{\mathrm{h}} = \dot{m}_{\mathrm{in}} - \dot{m}_{\mathrm{out}} \end{cases} \tag{1}$$

where $\alpha = {}^{K}/_{(\rho C_P)}$.

Typical values for the parameters entering the equations are reported in Table 2.

The first and the second equations in Sys. (1) describe the heat diffusion within the liquid and the

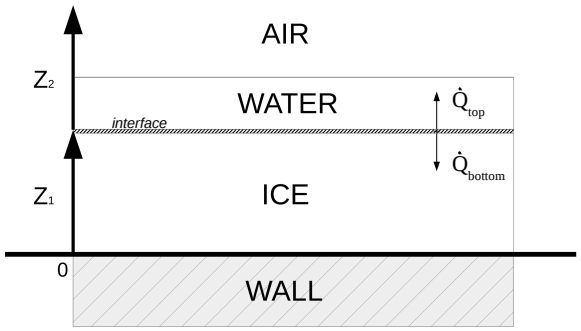

Fig. 1 Elementary cell and reference frames for the discrete Stefan problem (Sys. (1)).

solid phases, respectively, with z_1 and z_2 (cf. Fig. 1) indicating the direction normal to the surface. The third equation is the so-called Stefan condition; it enforces heat-flux balance at the solid-liquid interface. The fourth equation is the continuity equation, which enforces mass conservation. Under the assumption that the phase change occurs at an interface of infinitesimal thickness, the Stefan condition guarantees that the latent heat due to the phase change $\Delta\dot{Q}$ is equal to the net flux of heat towards the upper ($\dot{Q}_{\text{top}}$) and the lower ($\dot{Q}_{\text{bottom}}$) layers, see Fig. 1. The Stefan problem in the form of Sys. (1) is a moving-boundary problem: the positions of both the ice-water interface and of the liquid film surface vary with time and depend on the solution itself. No analytical solutions of the complete Stefan problem for the icing problem are currently available. The two icing models that will be presented in the next sections both introduce a number of assumptions leading to a simplified formulation of the complete problem described by Sys. (1).

B. Myers Model

Myers model [17] is obtained by applying a certain number of assumptions. First of all, the physical properties of ice and water (such as density or thermal conductivity) are assumed to be fixed at any condition of temperature and the phase change occurs at 273.15 K. In aeronautical application the thickness of the water film over the ice substrate is usually very small (less than 1/10 mm) [17] and, although in Myers the temperature profile within the water layer is shown to be linear with thickness, in practical applications it is acceptable to assume the temperature of the liquid film approximately constant and equal to the freezing temperature of water. Also the temperature of droplets is considered to be constant and equal to the free-stream temperature.

This is reasonable because droplets suspended within the cloud are in thermal equilibrium with the surrounding air. Finally, heat diffusion is supposed to be faster than ice accretion, therefore the time scale of the two processes are clearly separated. By introducing the above hypotheses, the Stefan problem simplifies to

$$\begin{cases} \dfrac{\partial T}{\partial t} = \alpha_{\mathrm{i}} \dfrac{\partial^2 T}{\partial {z_1}^2} \\ \dfrac{\partial \vartheta}{\partial t} = \alpha_{\mathrm{w}} \dfrac{\partial^2 \vartheta}{\partial {z_2}^2} \\ L_{\mathrm{f}} \rho_{\mathrm{i}} \dfrac{\partial B}{\partial t} = K_{\mathrm{i}} \left. \dfrac{\partial T}{\partial z_1} \right|_B - K_{\mathrm{w}} \left. \dfrac{\partial \vartheta}{\partial z_2} \right|_0 \\ \rho_{\mathrm{i}} \dfrac{\partial B}{\partial t} + \rho_{\mathrm{w}} \dfrac{\partial h}{\partial t} = \beta \, \mathrm{LWC} \, V_\infty \end{cases} \tag{2}$$

Myers derived two different accretion laws for rime and glaze ice and formulated a criterion based on the so-called *rime limit thickness* B_{g} to discern whether rime or glaze ice occurs.

1. *Rime ice limit thickness*

According to the Myers model, the so-called limiting thickness, namely the ice thickness at which water first appears, is defined as:

$$B_{\mathrm{g}} = \frac{A K_{\mathrm{i}} \left(T_{\mathrm{f}} - T_{\mathrm{w}} \right)}{A L_{\mathrm{f}} \beta \, \mathrm{LWC} \, V_\infty - \dot{Q}_{\mathrm{top}}} \tag{3}$$

The parameter B_{g} is computed by imposing $h = 0$ in the system of equations (2), as detailed in Ref. [17]. According to Myers model, rime ice forms if the limit thickness is negative or if B is smaller than B_{g}. If, instead, B is larger than B_{g}, glaze ice is formed.

2. *Rime ice conditions*

The hypothesis that the ice growth rate is significantly slower than the heat conduction rate through the ice layer leads to a substantial simplification of the problem. Namely, provided that the non-dimensional typical height of the ice layer satisfies

$$B(t) \ll \frac{K_{\mathrm{i}}}{\beta \, \mathrm{LWC} \, V_\infty C_{\mathrm{P_i}}} \tag{4}$$

the heat diffusion equation can be approximated to the leading-order quasi-steady problem

$$\frac{\partial^2 T}{\partial z_1^2} \approx 0 \tag{5}$$

From the values of K_i and $C_{\mathrm{P_i}}$ in Tab. table:parameters and assuming—following Myers [17]—a free-stream velocity of 90 m/s, a collection efficiency β of 0.55 and a cloud Liquid Water Content LWC of 0.001 g/m^3, the condition (4) translates into the requirement $\hat{B} \ll 2.4$ cm. The temperature profile within the ice layer can be retrieved by integrating Eq. (5) twice and imposing the boundary conditions

$$T = T_\mathrm{w} \qquad \text{at } z_1 = 0, \tag{6a}$$

$$\frac{\partial T}{\partial z_1} = \left(\dot{Q}_\mathrm{ci} + \dot{Q}_\mathrm{s} + \dot{Q}_\mathrm{d}\right) - \left(\dot{Q}_\mathrm{ai} + \dot{Q}_\mathrm{k} + \dot{Q}_\mathrm{l}\right) = \dot{Q}_\mathrm{top} \qquad \text{at } z_1 = B, \tag{6b}$$

where in the rime ice regime, the term $\dot{Q}_\mathrm{top}$ in Eq. (6b) is the total net amount of heat exchanged by the ice surface with the external airflow. The integration of the quasi-steady heat diffusion problem delivers to a linear variation of the temperature within the ice layer, which results in expression (7):

$$\dot{Q}_\mathrm{bottom} = K_\mathrm{i} \frac{\partial T}{\partial z_1} = K_\mathrm{i} \frac{T_\mathrm{f} - T_\mathrm{w}}{B} \tag{7}$$

The accretion rate in the rime regime can be immediately computed from the mass conservation equation, as

$$\frac{\partial B}{\partial t} = \frac{\beta \,\mathrm{LWC}\, V_\infty}{\rho_{\mathrm{i_{rime}}}} \tag{8}$$

3. Glaze ice conditions

In the glaze ice regime, the time scale separation argument addressed in the previous section leads to the quasi-steady form of the heat equations in the ice and water layers

$$\frac{\partial^2 T}{\partial z_1^2} \approx 0, \qquad \frac{\partial^2 \vartheta}{\partial z_2^2} \approx 0 \tag{9}$$

provided that

$$\hat{B} \ll \frac{K_\mathrm{i}}{(1-\phi)\beta \,\mathrm{LWC}\, V_\infty C_{\mathrm{P_i}}} \sim \frac{0.024}{(1-\phi)} \mathrm{m} \tag{10a}$$

$$\hat{h} \ll \frac{K_\mathrm{w}}{\phi\beta \,\mathrm{LWC}\, V_\infty C_{\mathrm{P_w}}} \sim \frac{0.003}{\phi} \mathrm{m} \tag{10b}$$

where ϕ is the fraction of the liquid water over the total water. In aeronautical applications, ϕ is usually well below unity. Moreover, in aircraft icing conditions the typical height of the liquid film

is of the order of $1/10$ mm. This allows another important simplifying assumption to be formulated: the conduction coefficient through the water film is infinite, so temperature in the water layer can be set as constant and equal to the freezing temperature of water. Therefore the Stefan condition yields the accretion law

$$\frac{\partial B}{\partial t} = \frac{1}{\rho_{i_{\text{glaze}}} L_{\text{f}}} \left(\dot{Q}_{\text{bottom}} + \dot{Q}_{\text{top}} \right) \tag{11}$$

where

$$\dot{Q}_{\text{top}} = \left(\dot{Q}_{\text{cw}} + \dot{Q}_{\text{e}} + \dot{Q}_{\text{d}} \right) - \left(\dot{Q}_{\text{aw}} + \dot{Q}_{\text{k}} \right) \quad \text{at} \quad z_2 = h, \tag{12}$$

represents the total net amount of heat exchanged between the water film and the external flow. Integrating twice Eq. (9), complemented with the boundary conditions (6a) and

$$T(B,t) = \vartheta(0,t) = T_{\text{f}}, \tag{13}$$

a linear temperature profile in the ice layer is finally obtained as follows:

$$T(z_1) = T_{\text{w}} + \frac{T_{\text{f}} - T_{\text{w}}}{B} z_1 \tag{14}$$

C. Local solution to the unsteady Stefan problem

In the present section, the new ice accretion model is presented. In the rime ice regime, the new model closely follows Myers formulation. However, differently from the original model, it introduces a source term accounting for mass transfer occurring from a glaze cell to an adjacent rime cell and for mass leaving the control volume due to sublimation (Sec. II C 2). In the glaze ice regime, the new model departs from the original one in that it introduces an unsteady treatment of the heat diffusion problem through the ice layer (Sec. II C 3). The local temperature of the airflow is also considered to evaluate the heat exchanged by convection at the water-air interface.

1. *Local temperature*

The ice accretion problem is very sensitive to the airflow temperature: indeed, a change of few degrees in air temperature can lead to very different ice formations. Also, an accurate description of the temperature field is key to evaluate the heat fluxes in balance equations. In diverse flight

conditions, the air temperature over the surface is different from point to point because air is a compressible fluid which is subjected to temperature variation related to local changes in pressure and density. This variation is therefore strictly related to the velocity field around the body, and it plays a key role at subsonic velocities. According to the boundary layer approximation, in the absence of shock waves, both the total enthalpy and the entropy are constant outside the boundary layer. As a consequence, regions with higher velocities are related to lower temperatures and vice versa. The maximum value of temperature is reached at the stagnation point because there the flow has zero velocity.

The term *local temperature* refers here to the air temperature near the surface just outside the thermal boundary layer whose thickness (δ_T) is related to that of the viscous boundary layer (δ_ν) through the Prandtl number ($\mathrm{Pr} = \nu/\alpha$) with the relation $\delta_\nu \approx \mathrm{Pr}^{1/3}\delta_\mathrm{T}$. A typical value of Prandtl number in air and subsonic conditions is around $0.7 \backsim 0.8$, so $\delta_\mathrm{T} \approx \delta_\nu$. In this conditions it is therefore acceptable to consider the *local temperature* as the temperature of air just outside the viscous boundary layer. Taking into account compressibility effects, the local temperature field is recovered from the isentropic relation for an ideal, diluted gas with constant specific-heat ratio γ as follows

$$\frac{P}{P_0} = \left(\frac{T}{T_0}\right)^{\frac{\gamma}{\gamma-1}} \qquad \rightarrow \qquad T = T_0 \left(\frac{P}{P_0}\right)^{\frac{\gamma-1}{\gamma}} \tag{15}$$

where under the further assumption that the total specific enthalpy is constant, $h^t = h + \dfrac{V^2}{2} = \text{const}$, the stagnation quantities T_0 and P_0 are computed from free-stream conditions as

$$T_0 = T_\infty + \frac{V_\infty^2}{2c_\mathrm{p}} \tag{16a}$$

$$P_0 = P_\infty \left(1 + \frac{\gamma-1}{2} M_\infty^2\right)^{\dfrac{\gamma}{\gamma-1}} \tag{16b}$$

Fig. 2 shows the contours of the difference between the free-stream and the local air temperature for the value of the test case conditions reported in Tab. 3. The difference between the maximum and the minimum temperature is around 6 degrees after 360 seconds, in particular the local temperature is less than the asymptotic one near the tip of the two horns and larger near the stagnation point.

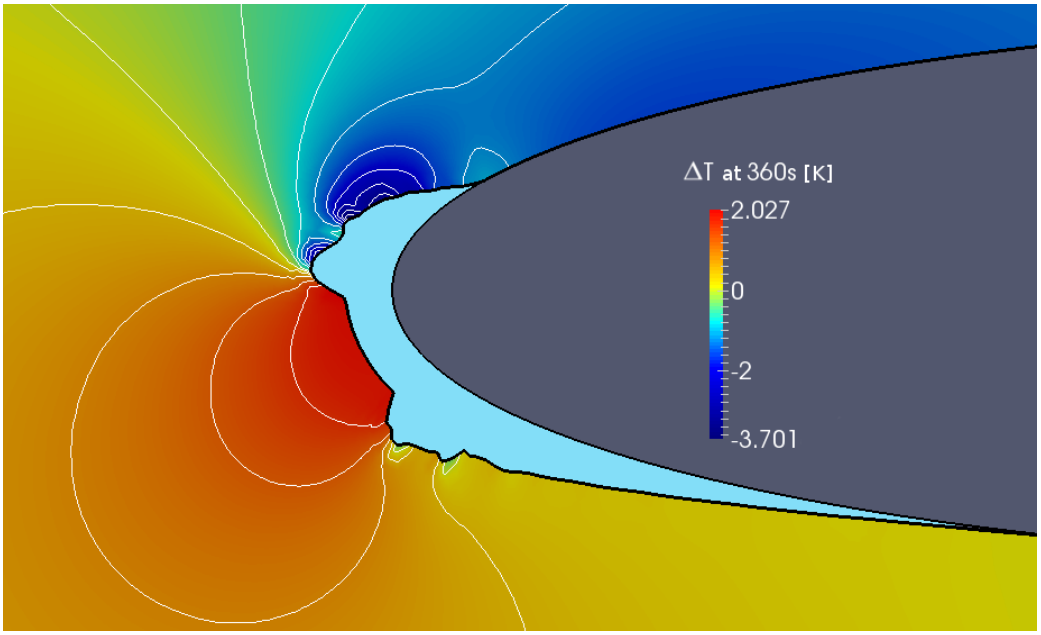

Fig. 2 Difference between the free-stream static temperature and the local temperature field around an iced airfoil.

Table 3 Flight conditions for the reference case.

α [deg]	V_∞ [m/s]	T_∞ [K]	P_∞ [Pa]	chord [m]
4	67	267.6	95000	0.53

The value of the *local temperature* correction affects the convective heat flux, the evaporation heat flux and the sublimation heat flux. Differently from Myers model, the local value of temperature is used in place of the free-stream value for the computation of such heat fluxes. In particular:

$$\dot{Q}_\mathrm{c} = h_\mathrm{c}(T - T_\infty)\, A \quad \longrightarrow \quad \dot{Q}_\mathrm{c} = h_\mathrm{c}\,(T - T_\mathrm{local})\; A \tag{17a}$$

$$\dot{Q}_\mathrm{e,s} = \chi_\mathrm{e,s}\; e_0\,(T - T_\infty)\; A \quad \longrightarrow \quad \dot{Q}_\mathrm{e,s} = \chi_\mathrm{e,s}\; e_0\,(T - T_\mathrm{local})\; A \tag{17b}$$

2. Rime ice conditions

The same arguments leading to Eq. (7) in Sec. II B 2 still hold. In the present formulation, a different accretion rate which explicitly accounts for the mass flux related to sublimation and allows

mass transfer from glaze cells to rime cells is introduced (cf. Eq. (8))

$$\frac{\partial B}{\partial t} = \left[\frac{\dot{m}_{\mathrm{d}} + \dot{m}_{\mathrm{in}} - \dot{m}_{\mathrm{s}}}{A \rho_{\mathrm{i_{rime}}}} \right] \tag{18}$$

The term $\dot{m}_{\mathrm{s}} = \dot{Q}_{\mathrm{s}} / \dot{L}_{\mathrm{s}}$, is the mass flux leaving the rime cell due to sublimation, whereas $\dot{m}_{in}$ is the mass of water flowing from an adjacent glaze cell, if any exists. In Eq. (18), no outward mass flux is included, except for $\dot{m}_{\mathrm{s}}$, since in the rime ice regime the total amount of incoming water is supposed to freeze.

3. Glaze ice conditions

As observed in Sec. II B 3, the quasi-steady hypothesis for the heat diffusion problem holds if Eq. (10) is satisfied. As a consequence, the heat diffusion equations within the ice layer is reduced from a Partial Differential Equation (Eq. 1 of Sys. (2)) to an Ordinary Differential Equation (Eq. (9)) and the resulting temperature profile is linear. However, in peculiar conditions involving rapid altitude variations or Super-cooled Large Droplet impact, large ice accretion rate are expected and the quasi-steady hypothesis (10) is possibly violated. Moreover, the hypothesis of isothermal wall is not consistent with the linear temperature profile assumption in the ice layer.

The quasi-steady assumption for the temperature profile and the isothermal wall assumption are now removed to solve these inconsistencies and to allow an unsteady behavior of the temperature within the ice layer. The starting point of the proposed formulation is again the Stefan problem Eq. (2).

In the present formulation, thanks to the constant liquid-film temperature hypothesis discussed in Sec. II B, the temperature profile within the liquid layer is not explicitly solved. A Dirichlet boundary condition is imposed at the ice-liquid interface, where the temperature is equal to the fusion temperature, and at the wall, where the temperature is equal to the surface temperature of the body as follows

$$T(0,t) = T_{\mathrm{w}} \qquad \text{and} \qquad T(B(t),t) = T_{\mathrm{f}} \tag{19}$$

The Neumann boundary condition (12) is imposed at the liquid water-air interface. Under these

assumptions, the Stefan problem reduces to

$$\begin{cases} \dfrac{\partial T}{\partial t} = \alpha_{\mathrm{i}} \dfrac{\partial^2 T}{\partial z_1^2} \\ \\ \rho_{\mathrm{i}} L_{\mathrm{f}} \dfrac{\partial B}{\partial t} = -K_{\mathrm{w}} \dfrac{\partial \vartheta}{\partial z_2}\bigg|_0 + K_{\mathrm{i}} \dfrac{\partial T}{\partial z_1}\bigg|_B \end{cases} \tag{20}$$

An unsteady exact solution for the above simplified Stefan problem is sought using a similarity approach to determine the temperature profile in the ice layer and, consequently, the glaze ice accretion rate. Solving the Fourier equation in the ice layer by means of a similarity solution requires the temperature at the wall and at the ice-water interface to be specified [21]. The heat diffusion equation in the ice layer is a PDE in space and time, and it is here reduced to an ODE by introducing the definition of the following similarity variable

$$\xi(z_1, t) = \frac{z_1}{\sqrt{t}} \tag{21}$$

The temperature within the ice layer, expressed in terms of the similarity variable ξ, is referred to as:

$$T(z_1, t) = \Theta(\xi(z_1, t))$$

The time and space derivatives of $T(z_1, t)$ are expressed as function of ξ as:

$$\frac{\partial T}{\partial t} = -\frac{z_1}{2t\sqrt{t}} \frac{\mathrm{d}\Theta}{\mathrm{d}\xi} = -\frac{\xi}{2t} \frac{\mathrm{d}\Theta}{\mathrm{d}\xi} \tag{22a}$$

$$\frac{\partial^2 T}{\partial z_1^2} = \frac{1}{t} \frac{\mathrm{d}^2\Theta}{\mathrm{d}\xi^2} \tag{22b}$$

Substituting the temperature derivatives from Eq. (22) into the first equation of system (20), the heat equation in the ice layer for $t > 0$ reduces to the ODE:

$$\frac{\mathrm{d}^2\Theta}{\mathrm{d}\xi^2} + \frac{1}{2} \frac{\xi}{\alpha_{\mathrm{i}}} \frac{\mathrm{d}\Theta}{\mathrm{d}\xi} = 0 \tag{23}$$

The well-known solution of this ODE reads:

$$\Theta(\xi) = A \int_0^{\xi} \exp\left(-\frac{s^2}{4\alpha_{\mathrm{i}}}\right) \mathrm{d}s + D = A \,\mathrm{erf}\left(\frac{\xi}{2\sqrt{\alpha_{\mathrm{i}}}}\right) + D \tag{24}$$

where A and D are the integration constants determined applying the boundary conditions (19):

$$\Theta(0) = T(0, t) = T_{\mathrm{w}} \quad \longrightarrow \quad D = T_{\mathrm{w}} \tag{25a}$$

$$\Theta\left(\frac{B(t)}{\sqrt{t}}\right) = T\left(B(t), t\right) = T_{\mathrm{f}} \quad \longrightarrow \quad A = \frac{T_{\mathrm{f}} - T_{\mathrm{w}}}{\mathrm{erf}\left(\lambda\right)} \tag{25b}$$

and where the new function $\lambda(t)$ is introduced as

$$\lambda(t) = \frac{B(t)}{2\sqrt{\alpha_i t}} \tag{26}$$

Substituting A and D from Eq. (25) and the definition of ξ (Eq. (21)) into Eq (24), the exact temperature profile within the ice layer yields

$$T(z_1, t) = T_w + (T_f - T_w) \frac{\text{erf}\left(\frac{z_1}{2\sqrt{\alpha_i t}}\right)}{\text{erf}\,(\lambda)} \tag{27}$$

However, the temperature profile described by Eq. (27) cannot be replaced immediately into the governing equations because it still depends on the position of the ice-water interface $B(t)$, which appears in the definition of the parameter $\lambda(t)$ (Eq. (26)) which it is still unknown. The procedure to retrieve $\lambda(t)$, $B(t)$ and $\partial B/\partial t$ is here explained. The parameter $\lambda(t)$ is derived from the Stefan condition (Eq. (20) b) after the ice accretion rate and the heat fluxes across the interface are substituted in it. First of all the ice accretion rate is derived from Eq. (26). The position of the water-ice interface reads

$$B(t) = 2\lambda(t)\sqrt{\alpha_i t} \tag{28}$$

and the accretion rate can thus be expressed as function of $\lambda(t)$

$$\frac{dB}{dt} = \lambda(t)\sqrt{\frac{\alpha_i}{t}} + 2\frac{d\lambda}{dt}\sqrt{\alpha_i t} \tag{29}$$

The procedure and the hypotheses adopted to derive the temperature gradient at the water-ice interface follow the original procedure proposed by Myers in Ref. [17]. For conciseness, the final result is:

$$-\left.\frac{\partial \vartheta}{\partial z_2}\right|_0 \approx \frac{\left(\dot{Q}_{ci} + \dot{Q}_s + \dot{Q}_d\right) - \left(\dot{Q}_{ai} + \dot{Q}_k + \dot{Q}_l\right)}{K_w} = \frac{\dot{Q}^*_{top}}{K_w} \tag{30}$$

Note that the $\dot{Q}^*_{top}$ is referred to the sum of the heat fluxes computed including the local temperature correction introduced in Sec. II C 1.

The temperature gradient at the ice-water interface is obtained from the derivative of the exact temperature profile in the ice layer (Eq. (27))

$$\frac{\partial T}{\partial z_1} = \frac{(T_f - T_w)}{\text{erf}\,(\lambda)} \frac{\exp\left(-\left(\frac{z_1}{2\sqrt{\alpha_i t}}\right)^2\right)}{\sqrt{\pi \alpha_i t}}$$

which evaluated at $z_1 = B$ is:

$$\left.\frac{\partial T}{\partial z_1}\right|_B = \frac{(T_\mathrm{f} - T_\mathrm{w})}{\mathrm{erf}\,(\lambda)} \frac{\exp\left(-\lambda^2\right)}{\sqrt{\pi \alpha_\mathrm{i} t}} \tag{31}$$

Substituting Eq. (29), Eq. (30) and Eq. (31) into the second equation of Sys. (20), the Stefan condition is written as the following alternative non-linear ODE equation in the unknown $\lambda(t)$

$$\frac{\mathrm{d}\lambda(t)}{\mathrm{d}t} + \frac{1}{2}\frac{\lambda(t)}{t} - \frac{K_\mathrm{i}}{2\sqrt{\pi}} \frac{(T_\mathrm{f} - T_\mathrm{w})}{L_f \rho_i \alpha_\mathrm{i}} \frac{\exp\left(-\lambda(t)^2\right)}{t\,\mathrm{erf}\,(\lambda(t))} - \frac{\dot{Q}^*_\mathrm{top}}{2 L_f \rho_i \sqrt{\alpha_\mathrm{i} t}} = 0 \tag{32}$$

where the initial condition for equation (32) is computed from the definition (28) as

$$\lambda(t_0) = \frac{B(t_0)}{2\sqrt{\alpha_\mathrm{i} t_0}} \tag{33}$$

where t_0 is the time at which glaze ice occurs first. An explicit Euler method is also used for the solution of (32). From the value λ_n at time $t = t_n$, the thickness of the ice layer at each time step is calculated by means of an explicit Euler algorithm

$$B_{n+1} = B_n + \left.\frac{dB}{dt}\right|_n \Delta t \tag{34}$$

where from definition (29) one has

$$\left.\frac{\partial B}{\partial t}\right|_n = \frac{1}{\rho_i\, L_f} \left(K_\mathrm{i} \frac{(T_\mathrm{f} - T_\mathrm{w})}{\mathrm{erf}\,(\lambda_n)} \frac{\exp\left(-\left({\lambda_n}^2\right)\right)}{\sqrt{\pi \alpha_\mathrm{i} t_n}} + \dot{Q}^{*\,(n)}_\mathrm{top} \right) \tag{35}$$

During the first time-step the ice is assumed to grow in the rime regime, so the ice thickness B_0 is always known.

The exact temperature profile (27) simplifies to Myers' one (cf. (14)) for $t \to +\infty$ (steady conditions), as follows. Both argument of the $\mathrm{erf}\,(x)$ function tend to zero for $t \to \infty$, since $z_1 \in [0, B(t)]$ and λ in (26) tend to zero because $B(t)$ tend to a finite value as $t \to \infty$.

It is possible to approximate the error function using the well-known Taylor series expansion as follows

$$\mathrm{erf}\,(x) \simeq \frac{2}{\sqrt{\pi}} \sum_{n=0}^{\infty} \frac{(-1)^n x^{2n+1}}{n!(2n+1)} = \frac{2}{\sqrt{\pi}} \left(x - \frac{x^3}{3} + \frac{x^5}{10} - \frac{x^7}{42} + \frac{x^9}{216} - \cdots \right) \qquad \text{for } x \to 0$$

to obtain

$$\mathrm{erf}\left(\frac{z_1}{2\sqrt{\alpha_\mathrm{i} t}}\right) \simeq + \frac{2}{\sqrt{\pi}} \left(\frac{z_1}{2\sqrt{\alpha_\mathrm{i} t}}\right) + o\left(t^{-\frac{1}{2}}\right) \qquad \text{for } t \to +\infty \tag{36a}$$

$$\mathrm{erf}\left(\frac{B(t)}{2\sqrt{\alpha_\mathrm{i} t}}\right) \simeq + \frac{2}{\sqrt{\pi}} \left(\frac{B(t)}{2\sqrt{\alpha_\mathrm{i} t}}\right) + o\left(t^{-\frac{1}{2}}\right) \qquad \text{for } t \to +\infty \tag{36b}$$

Table 4 Values of the accretion rates used in Fig. 3.

Case	Time $[s]$	Ice thickness $[m]$	Mean accretion rate $[m/s]$
(a)	100	0.02	$2 \cdot 10^{-4}$
(b)	200	0.02	$1 \cdot 10^{-4}$
(c)	300	0.02	$0.6 \cdot 10^{-4}$
(d)	400	0.02	$0.5 \cdot 10^{-4}$

Substituting Eq. (36a) and Eq. (36b) into Eq. (27), the resulting equation returns the same temperature profile obtained by Myers in glaze conditions (Eq. (14), Sec. II B 3):

$$T(z_1, t) \simeq T_{\mathrm{w}} + \frac{(T_{\mathrm{f}} - T_{\mathrm{w}})}{B(t)} z_1 \qquad \text{for } t \to +\infty$$

Different test cases are now considered to assess the dependence of the exact temperature profile (27) on the ice accretion rate. These conditions are summarized in Table 4 and are obtained by imposing a fixed value of the ice thickness and different accretion times, to modify the accretion rate.

As expected, Fig. 3 shows that the exact temperature profiles collapse to the Myers' linear one for small values of accretion rate. On the contrary, profiles become more and more different as the accretion rate increases. Fig. 3 reveals that the departure from linear behavior affects especially the values of the temperature derivative at the wall and at the ice-water interface. The first one represents the heat flux conduced away through the wall, whereas the second one is related to the speed at which the interface moves. The percentage difference between the derivative values computed with the compared models is reported in Table 5.

This difference is defined as:

$$\Delta_{\%} = \frac{T'_{\mathrm{Myers}} - T'_{\mathrm{exact}}}{T'_{\mathrm{Myers}}} \tag{37}$$

where the temperature derivatives depend on the model.

4. Rime ice limit thickness

Following Myers' approach [17], the criterion allowing to discern whether the rime or glaze accretion law is to be employed is based on the definition of the rime limit thickness. As already

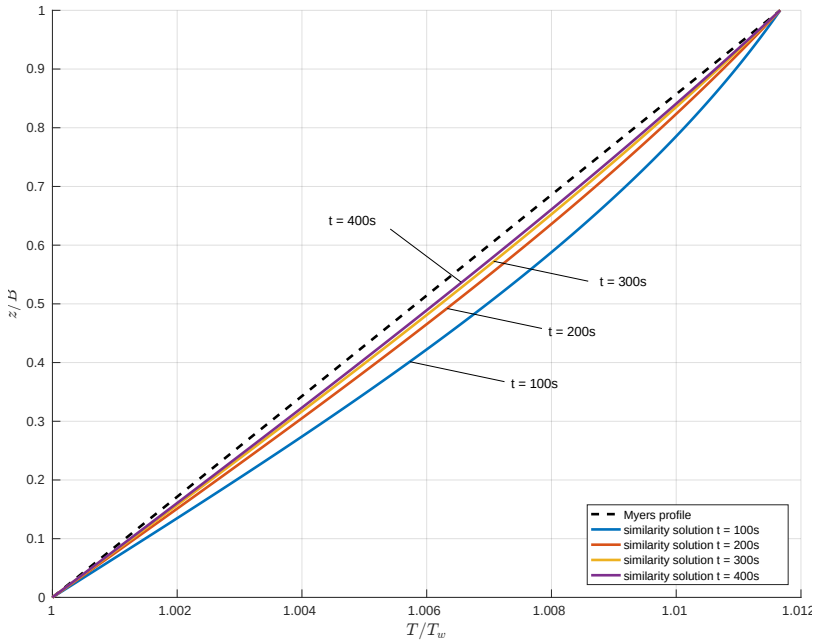

Fig. 3 Comparisons between the temperature profiles predicted by the Myers model (dashed line) and the exact unsteady model (continuous lines) within the ice layer.

Table 5 Percentage variation between temperature derivatives.

Case	$\Delta_{\%}{}^{\text{wall}}$	$\Delta_{\%}{}^{\text{interf.}}$
(a)	-28.04%	$+44.05\%$
(b)	-13.95%	$+24.67\%$
(c)	-9.27%	$+17.08\%$
(d)	-6.94%	$+13.05\%$

discussed in Sec. II B, the rime limit thickness B_g is the maximum rime ice thickness, beyond which only glaze ice can accrete.

III. Numerical results

PoliMIce is a highly modular ice accretion simulation framework developed at the Department of Aerospace Science and Technology of Politecnico di Milano [15]. A dedicated ice accretion module is coupled with diverse open-source and commercial CFD solvers to tackle two-dimensional and fully three-dimensional ice accretion problems. With reference to Fig. 4, the present section briefly summarizes the ice accretion calculation procedure.

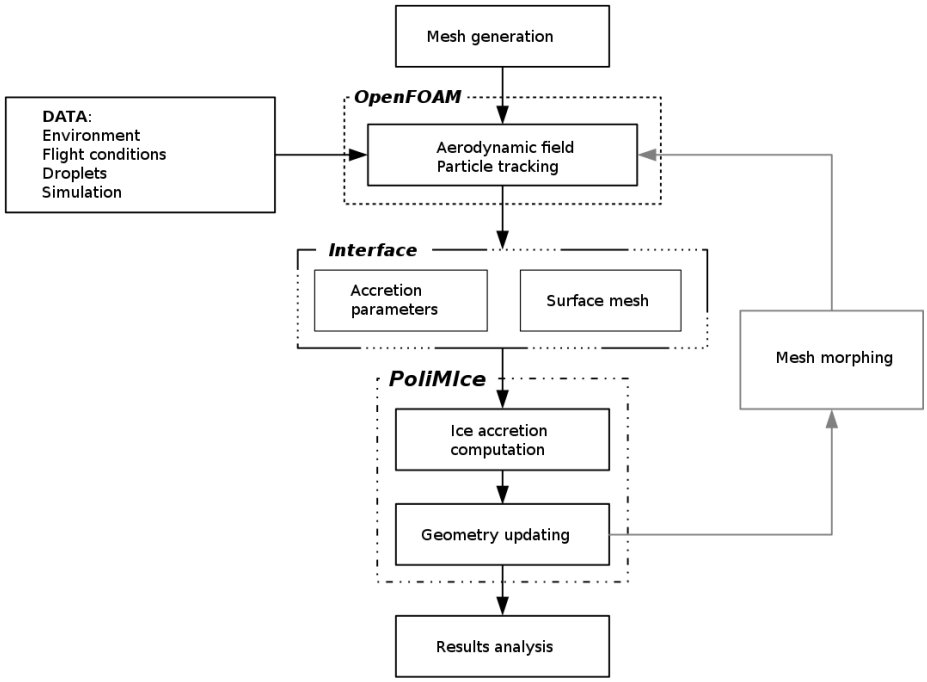

Fig. 4 Flowchart of calculation procedure within the PoliMIce framework.

The numerical procedure follows a well-established pattern which is commonly found in ice prediction codes (see e.g. Ref. [9]). Besides the baseline geometry, the definition of the icing problem requires diverse input parameters regarding flight and environmental conditions: total icing exposure time, free-stream velocity $\vec{V}_\infty$, ambient temperature T_a, droplet Median Volume Diameter (MVD) [1, 22] and Liquid Water Content (LWC) of the cloud (grams of water contained in a cubic meter of air).

Once the aerodynamic computational mesh is created and input data are set, the aerodynamic solver computes the flow-field around the body (block *OpenFOAM: Aerodynamic field* in Fig. 4) and a particle tracking solver determines the trajectories of water droplets (block *OpenFOAM: Particle tracking* in Fig. 4). In the present work, two solvers included in the open-source CFD suite OpenFOAM [23] are adopted, namely the aerodynamic solver *simpleFoam*, complemented with Spalart-Allmaras turbulence model [24, 25], and the Lagrangian particle tracking solver *uncoupledKinematicParcelFoam*.

A thermal analysis is needed to compute the thickness of the iced layer and depends on many parameters. The most important ones are the water distribution over the surface of the body, the

recovery factor and the heat transfer coefficient. The water distribution over the body surface is expressed through the so-called *collection efficiency* β, defined as the fraction of water impacting on each elementary portion of the surface over the free-stream concentration[1]. As far as the recovery factor and the heat transfer coefficient are concerned, CFD simulations showed that these quantities are approximately uniform within the flow-field. This does not hold in the laminar regime—which is relevant for the clean surface only—and in very small regions close to the leading edge. Results presented in this work were obtained assuming constant values for the heat transfer coefficient and the recovery factor over the entire domain, namely 1000 $\mathrm{W/m^2K}$ and 0.8. Finally, according to the thin film approximation, the wall shear stress drives the free water surface, in that it represents the sole external force acting on the film.

A C++ interface between the CFD/Lagrangian solver and the ice accretion module is used to recover the surface mesh from the volume mesh (block *OpenFOAM: Surface mesh* in Fig. 4). Accretion parameters are evaluated on the surface grid: water distribution is reconstructed once the cloud droplet trajectories and the related impingement points are known (block *Accretion parameters* in Fig. 4). The wall shear stress is retrieved from the computed flow-field.

The one-dimensional ice accretion problem (detailed in Sec. II) is solved in the direction normal to each surface cell. As a result, a piece-wise constant representation of the accretion rate in the ice and water layers over the aircraft surface is obtained (block *PoliMIce: Ice accretion computation* in Fig. 4). The PoliMIce accretion module reshapes the new geometry to account for the accreted ice and a smoothing algorithm is invoked to fix any non-physical region that may possibly arise due to interpenetrations or cuts due to the displacement of surface nodes (block *PoliMIce: Geometry updating* in Fig. 4).

The ice, which progressively accumulates during the assigned exposure time, modifies the external aerodynamic flow field and hence the trajectories of cloud droplets and the resulting accretion parameters. To account for this, a multi-step procedure [26] is implemented: the iced geometry is periodically updated into the CFD/Lagrangian solver and accretion parameters are recomputed, until the total icing exposure time is reached. Such procedure highlights the existence of two different time scales: the aerodynamic and the ice accretion one. The former is the time scale during which

Table 6 Test conditions for the glaze ice test case.

α [deg]	V_∞ [m/s]	T_∞ [K]	P_∞ [Pa]	MVD [μm]	LWC [g/m^3]	Exposure [s]
4	58.1	269.1	95600	20	1.3	480

significant variations in the aerodynamic performances due to shape modification are attained, while the latter is the characteristic time of the phase-changing problem, namely the time scale governing the ice growth.

As a final step, the CFD computational grid is adapted to the iced surface (block *Mesh morphing* in Fig. 4). This critical operation is performed applying the Inverse Distance Weighting (IDW) method proposed by D. Shepard in Ref. [27].

Exemplary test cases regarding both rime and glaze ice accretion over two-dimensional airfoils are now presented and discussed. Test conditions were chosen to verify the critical aspects of the novel icing model. In particular, the atmospheric temperature for the first test case in III A is slightly lower than that of ice melting point, thus being representative of conditions where ice grows mostly as *glaze* type. Test case showed in III B is instead exemplifying the opposite circumstances, i.e. *rime* ice accretion is prevailing over the airfoil. Results are compared against predictions from other ice accretion solvers and against experimental results. Only two-dimensional problems are considered, since ice shapes can be easily compared to available simulations and experimental results.

A. Glaze ice accretion

A NACA 0012 airfoil flying in environmental conditions promoting the formation of *glaze* ice is now considered. Data and parameters defining test conditions are resumed in Table 6. Further details about this test, as well as information regarding the experimental set up, can be found in Ref. [28].

Results from the original Myers model, and from the icing model proposed in this work are compared against the experimental shape, from Ref. [28], in Fig. 5. An analysis of the heat fluxes is given at the end of this paragraph. The total exposure time is 480 s and the flow-field update interval is 10 s. With reference to Fig. 5, experimental results evidence a large ice structure on the upper

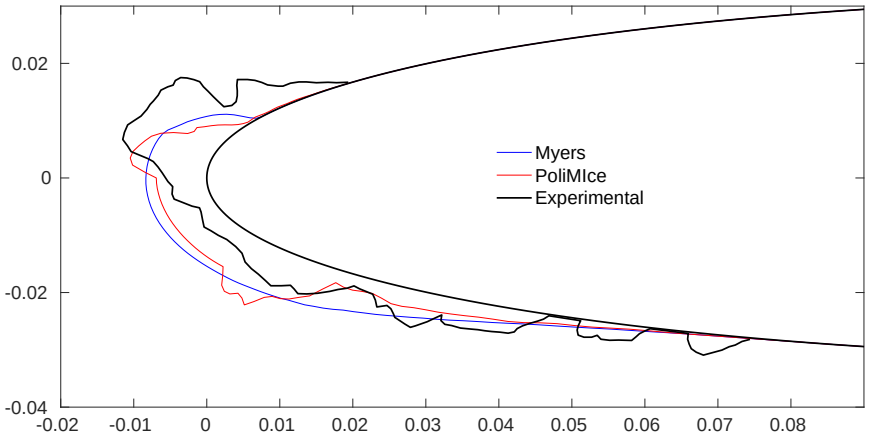

Fig. 5 Comparison between the PoliMIce prediction against the original Myers model and the experimental ice shape from Ref. [28]. Axes dimensions are in meters.

portion of the leading edge and ice formation on the lower portion that extends for about 0.08 m from the leading edge (airfoil chord is 0.53 m). The Myers model predicts a quite regular and smooth shape and the system of highly complex ice structures is loosely represented (Fig. 5). Moreover, in the region close to the stagnation point the final ice layer thickness is overestimated. The proposed model instead matches the experimental results more closely and it predicts the occurrence of the ice structure protruding from the leading edge. The size of this latter is however poorly captured. The ice thickness at the stagnation point is sightly closer to the experimental results (Fig. 6(c)).

With particular reference to the estimation of the ice thickness in the close proximity of the stagnation point, both modifications that were introduced with respect to the Myers model – the unsteady solution of the heat diffusion problem and the local temperature correction – contribute to provide more accurate predictions.

Figures 6(a) and 6(c) show a comparison of the ice shapes predicted by the Myers and the new model, respectively, in the case of uniform or variable air temperature distributions outside the boundary layer. In both figures, the blue lines are the numerical ice shapes obtained by Myers and PoliMIce models, respectively, under the assumption of uniform air temperature. Red lines are the numerical ice shapes calculated including the effects of a local (variable) air temperature. Indeed, the inclusion of this simple correction is found to be beneficial for predicting the ice thickness at the stagnation point and the ice structure in the upper portion of the leading edge.

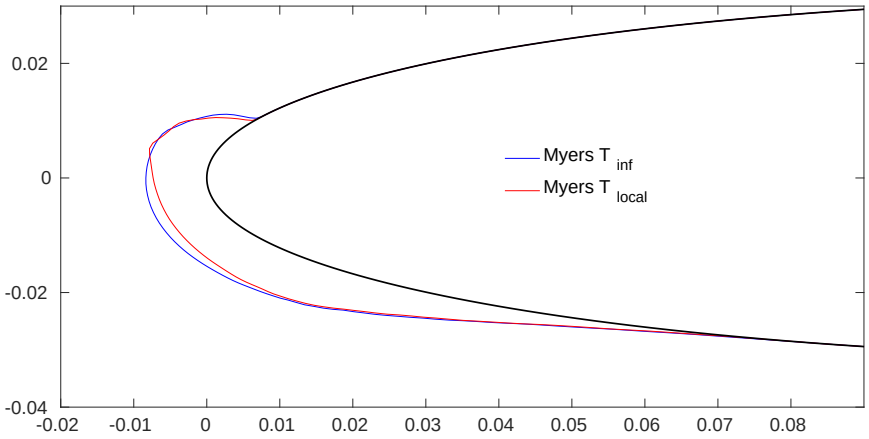

(a) Myers

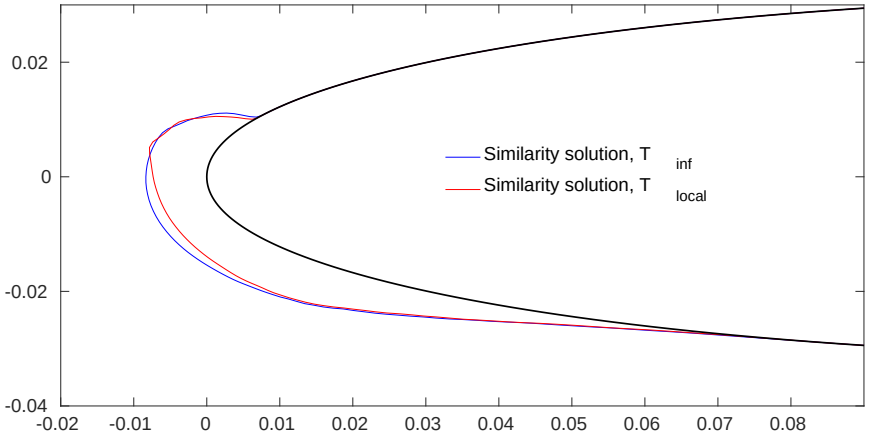

(b) Unsteady temperature correction

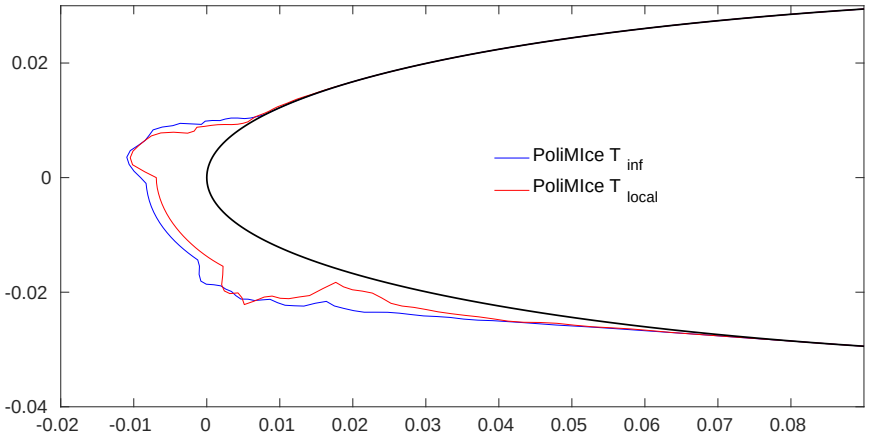

(c) PoliMIce

Fig. 6 Comparison of numerical results based on the free-stream temperature (blue lines) and the local temperature (red lines) for different icing models in glaze-ice conditions (Tab. 6). Axes dimensions are in meters.

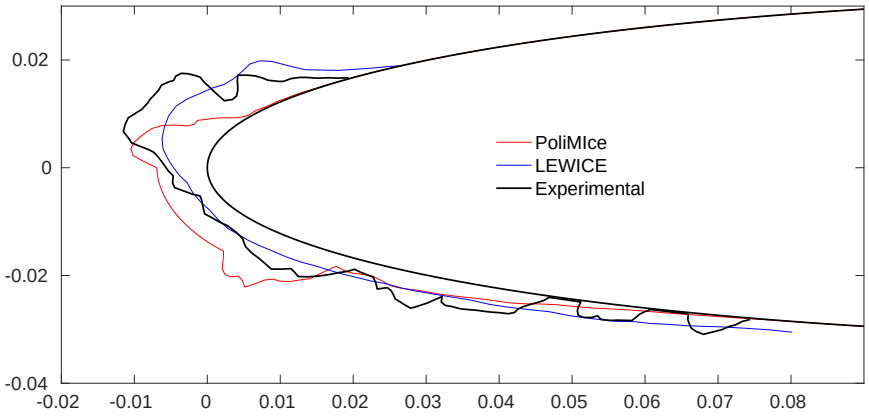

(a) LEWICE

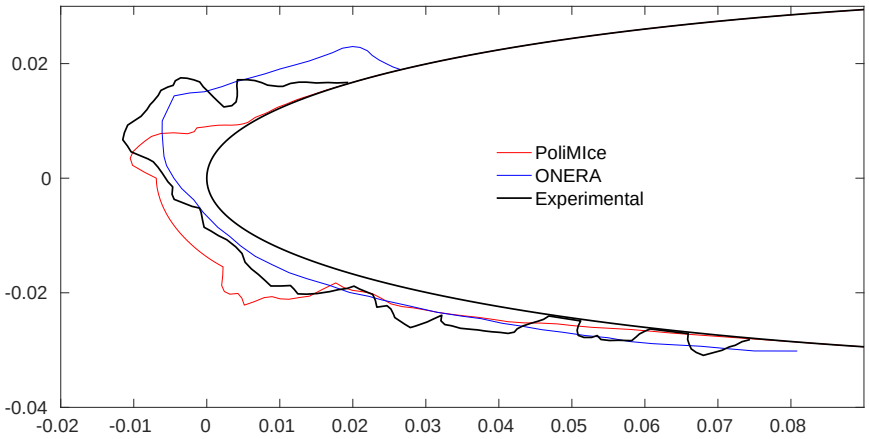

(b) ONERA

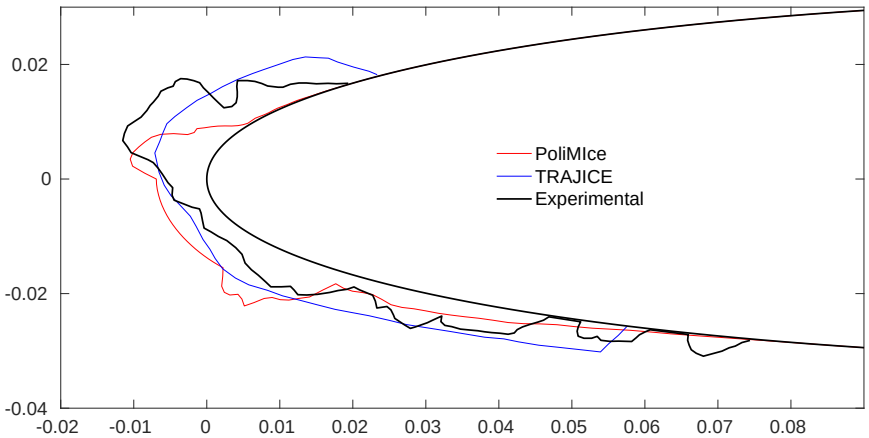

(c) TRAJICE

Fig. 7 Comparison between the PoliMIce prediction against the experimental ice shape from Ref. [28] and the LEWICE (a), the ONERA (b) and the TRAJICE (c) icing software. Axes dimensions are in meters.

The ability of representing irregular structures is possibly due to the inclusion of the $\dot{m}_{in}$ term in the rime ice accretion, as can be noticed by comparing Fig. 6(b) against Fig. 6(c), which differs only by the presence of this correction term. Indeed, ice is known to grow first as *rime* ice and then, after the thickness exceeds the B_g value, to continue growing as glaze ice: in general the B_g function has a relative minimum in the region close to the stagnation point. This is due to the collection efficiency distribution which, in general, reaches its maximum in the same cells. The higher amount of water hitting this portion of the surface causes *glaze* ice to appear initially there and hence the liquid film starts flowing over the airfoil towards the trailing edge along both the upper and the lower side. The film is driven by the action of the external air stream and, as a consequence, water flows downstream into the neighboring cells where lower value of β and T are observed. In this cells the value of B_g is hence higher and rime ice, which grows faster than glaze, occurs for a longer time thus producing the double-horn irregular shape. This process highlights the strong interaction between the local temperature and the $\dot{m}_{in}$ term correction.

As expected, Figures 6(a) and 6(b) shows that the inclusion of similarity solution does not provide a significant improvement, at least in this test condition.

Figure 7 reports a comparison of the present numerical results with those obtained by the LEWICE, ONERA and TRAJICE sofwtare. All these software overestimate the location of the ice-free region in the upper portion of the airfoil, which is however underestimated by the PoliMIce software. The LEWICE, ONERA and TRAJICE software also deliver a better estimate of the ice thickness at the stagnation point with respect to the present model. The ice shape predicted by the three software is very smooth, which possibly corresponds to the earlier occurrence of glaze ice. Note that the present model has no ambition to replace well-established ones implemented in ice-accretion codes. Rather, the present study focuses on understanding model limitations and the relevant parameters that influence ice accretion.

In this last part of the paragraph the heat fluxes involved in the current test case are analized. Heat fluxes are computed using the two models presented in Sec. II. In particular Eq. (38) and Eq. (39) are obtained evaluating the derivatives of the temperature profile $T(z_1, t)$ within the ice layer at wall in Myers and PoliMIce model, namely $q_{\mathrm{w}} = K_{\mathrm{i}} \left.\dfrac{\partial T}{\partial z_1}\right|_0$.

Rime ice:

$$q_{\mathrm{w}} = K_{\mathrm{i}} \left[\left(\dot{Q}_{\mathrm{ci}} + \dot{Q}_{\mathrm{s}} + \dot{Q}_{d} \right) - \left(\dot{Q}_{\mathrm{ai}} + \dot{Q}_{\mathrm{k}} + \dot{Q}_{\mathrm{l}} \right) \right] \tag{38}$$

Glaze ice:

$$\text{Myers:} \qquad q_{\mathrm{w}} = K_{\mathrm{i}} \frac{T_{\mathrm{f}} - T_{\mathrm{w}}}{B} \tag{39a}$$

$$\text{PoliMIce:} \qquad q_{\mathrm{w}} = K_{\mathrm{i}} \frac{1}{\sqrt{\pi \alpha_{\mathrm{i}} t}} \frac{(T_{\mathrm{f}} - T_{\mathrm{w}})}{\mathrm{erf}(\lambda)} \tag{39b}$$

Figure 8 shows the variation of the heat flux at the ice-airfoil interface over time computed using both Myers (Fig. 8 (a)) and PoliMIce model (Fig. 8 (b)). Heat fluxes were evaluated at 20, 40, 100 and 480 seconds. Both models reveal that the heat flux at wall decreases continuously in time. This happens because the growing ice layer acts as an insulator which gradually reduces the heat exchanged between the airfoil and the atmosphere. The shape of the heat profiles within the two figures are similar at every evaluated time except for the first one (at 20 seconds) where the behavior of the two models is significantly different. This discrepancy is due to a different ice regime around the stagnation point and, consequently, a different ice accretion law. The heat flux profile at 20 seconds in Fig. 8 (a) is typical of a full rime condition over the whole surface, whereas the corresponding profile in Fig. 8 (b) is typical of a surface including a glaze-ice region. In particular, the glaze-ice region is highlighted by a change in convexity, in this case a bowl between cells 95 and 112 appears.

Fig. 9 shows a comparison between heat fluxes 9(a) and ice thicknesses 9(b) computed by the Myers and the PoliMIce model after 40 seconds of ice accretion. The profiles of the heat fluxes and the ice thicknesses computed with both models are similar in term of shape and magnitude. In Fig. 9(a), both models give a bowl-shaped profile which indicates the presence of a glaze region. In the unsteady model this is slightly wider and shows two higher peaks. Fig. 9(b) shows that the unsteady model predicts a slightly higher maximum ice thickness at the stagnation point at this time, even though at the end of the simulation the Myers model predicts a thicker ice layer in the same place (Fig. 5). This behavior is due to the local temperature correction.

In Fig. 10 the components of the heat fluxes involved in the process after 40 seconds of ice

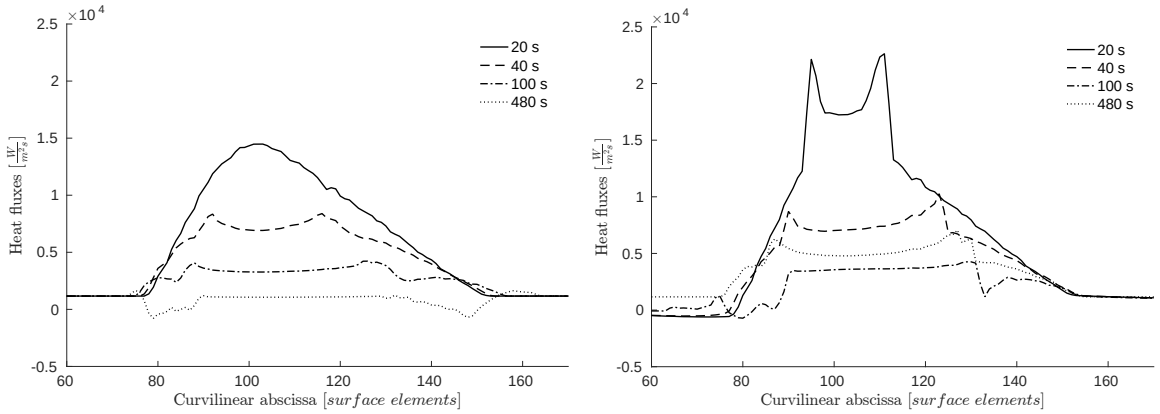

(a) Myers model

(b) PoliMIce model

Fig. 8 Heat fluxes based on the Myers (a) and the PoliMIce model (b) after different accretion times.

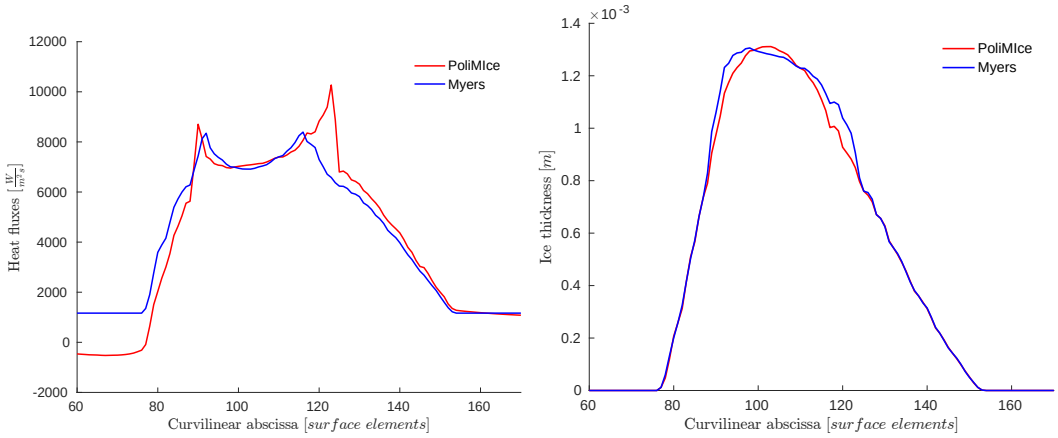

(a) Heat fluxes

(b) Ice thickness

Fig. 9 Heat fluxes and ice thickness based on the Myers and the PoliMIce models after 40 seconds of ice accretion.

accretion are detailed. The black bold line represents the heat flux at the wall: outside the dashed vertical lines the ice accretion is *rime* and the heat flux q_w follows Eq. (6b). In the region within the dashed lines, the accretion process is governed by the glaze equations (Eq. (39a) and (39b)). At the rime-glaze transition there is a discontinuity followed by a bowl the q_w profile. This behavior is due to the larger ice thickness near the stagnation point and, according to Eq. (39), this leads to a decrease of the heat fluxes. Fig. 10(b) reports the heat fluxes involved in the icing process and it is observed that the largest contributions are the latent and the convection heat fluxes, whereas the

Table 7 Flight conditions for the mixed rime-glaze ice test case.

α [deg]	V_∞ [m/s]	T_∞ [K]	P_∞ [Pa]	MVD [μm]	LWC [g/m^3]	Exposure [s]
1.5	128	263	125424	20	0.43	360

sublimation heat flux is negligible.

B. Mixed rime-glaze ice accretion

The test case presented in this section corresponds to the ice accretion over an aircraft wing while flying at very low temperature conditions for a significant time. Those conditions are favorable to the formation of *rime* ice and hence they are useful to assess the novel model in such conditions. The reader is referred to Ref. [29] for details regarding this test case and to Table 7 for a brief summary of the most relevant parameters. Fig. 11 shows the comparison between the ice predicted by the Myers and the PoliMIce models against the the experimental results. The mixed rime-glaze condition lead to the formation of a symmetrical double-horn structure. Since the ice accretion law in the *rime* regime differs from the Myers model only because of the inclusion of the $\dot{m}_{in}$ term, both models are expected to give very similar results if the temperature is well below zero, so that no glaze ice forms. This behavior is confirmed by comparing the ice profiles plotted in Fig. 12(a) and Fig. 12(c) (blue lines). Fig. 12(b) shows the ice shapes obtained by adding the unsteady temperature profile to Myers description. By comparing these shapes to those reported in Fig. 12(a) and 12(c), one should conclude that the prediction of the double-horn shape arises from the combination of both the local temperature and the rime rate corrections. As expected, the inclusion of similarity solution accounting for unsteadiness does not provide a significant improvement. Indeed, the similarity solution is introduced only in the *glaze* ice regime and in this case *glaze* ice appears only in the first stage of the simulation.

The local temperature correction affects in particular the area near the stagnation point. In this region the air static temperature is higher and produce a large amount of water that flows from the leading edge towards the trailing edge. Along its path the water experiments regions with lower air temperature, namely the regions where the surrounding air is accelerating, and the freezing process

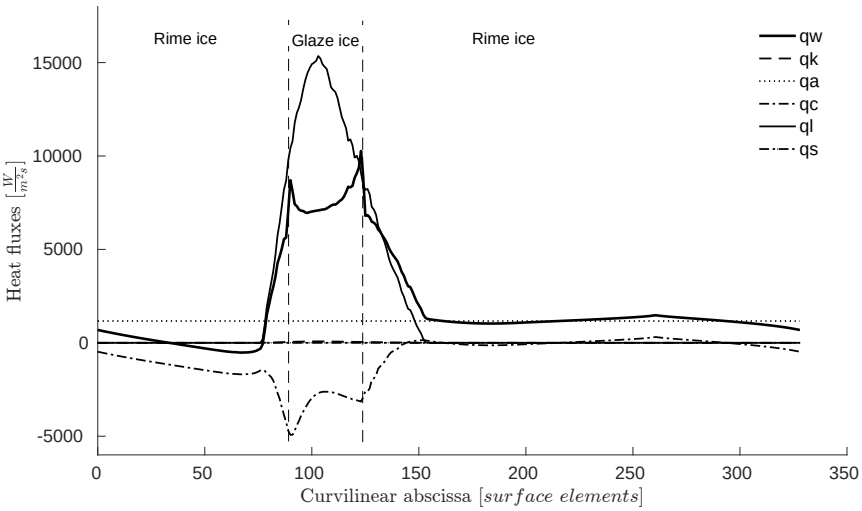

(a) Heat fluxes components

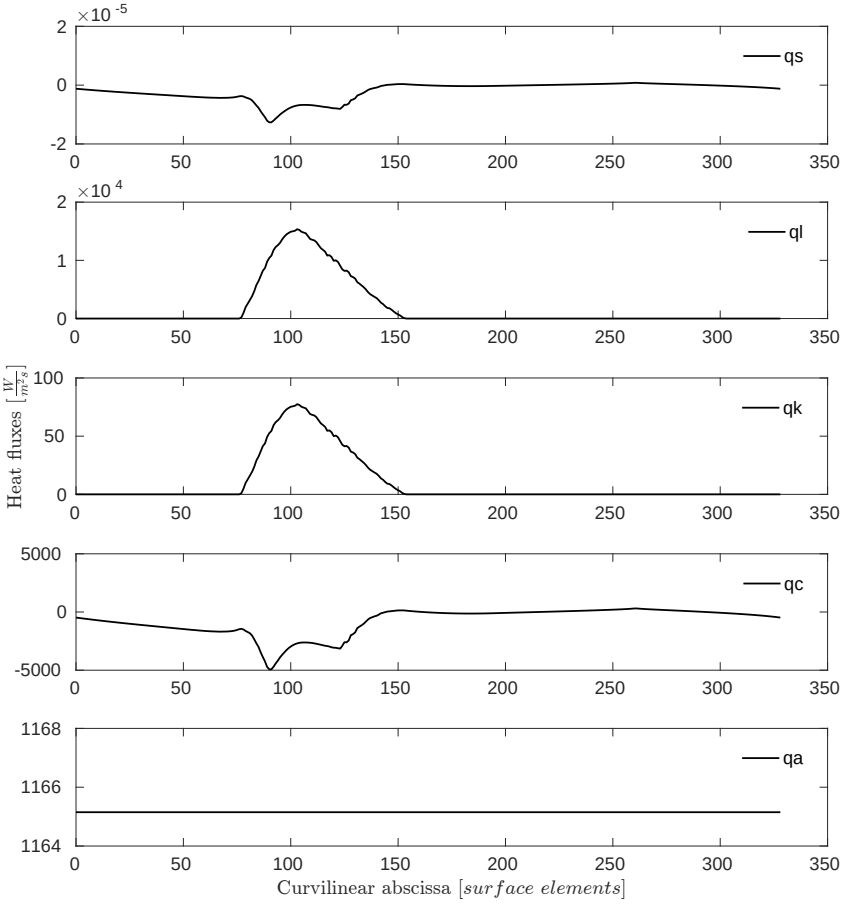

(b) Heat fluxes in details

Fig. 10 Wall heat fluxes based on the PoliMIce model (a) and the detail of each component involved in the process (b).

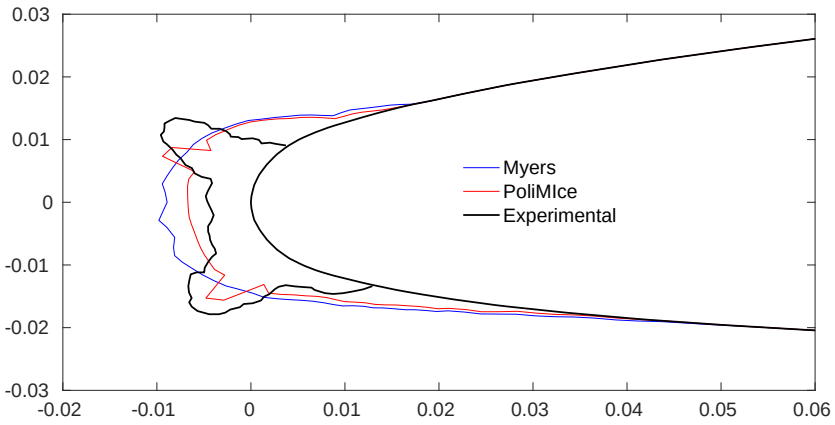

Fig. 11 Comparison between the PoliMIce prediction against the original Myers model and the experimental ice shape from Ref. [29]. Axes dimensions are in meters.

is facilitated. The interaction between the local temperature correction and the $\dot{m}_{in}$ correction leads to the formation of the double-horn ice structure. Without the rime rate correction, it would not be possible to take into account this additional water flow into account and the model cannot guarantee the conservation of the mass of water. In this respect, Myers model in the mixed rime-glaze regime is not conservative. With reference to Fig. 12(c), one can notice that, by introducing this correction into the rime law, the typical two-horn configuration is predicted to occur in the correct location, though its size is smaller than the one observed experimentally.

IV. Conclusions

A modification to the Myers model for predicting in-flight ice accretion was proposed and implemented in the ice accretion software PoliMIce developed at Politecnico di Milano. The new model is based on the exact solution of the unsteady Stefan problem to account for the effects of heat propagation within the ice layer. Numerical simulations over two-dimensional airfoil in both rime and glaze ice conditions were carried out to assess the accuracy of the model. Preliminary results suggest that the introduction of the new unsteady temperature profile does not significantly improve the accuracy of predictions in terms of ice thickness and shape, at least for the considered test cases. Improvements for both rime and glaze ice predictions were found to be mainly related to the correction of the rime accretion rate accounting for mass exchange from glaze to rime cells and to the introduction of the local value of the air temperature. The local air temperature was introduced

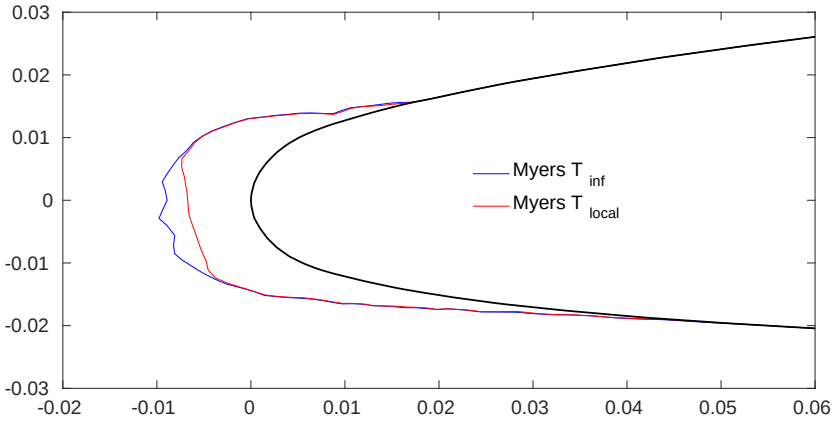

(a) Myers

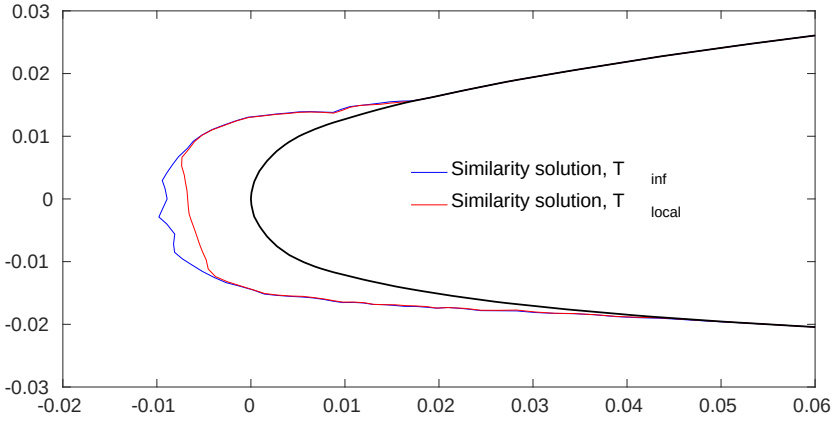

(b) Unsteady temperature correction

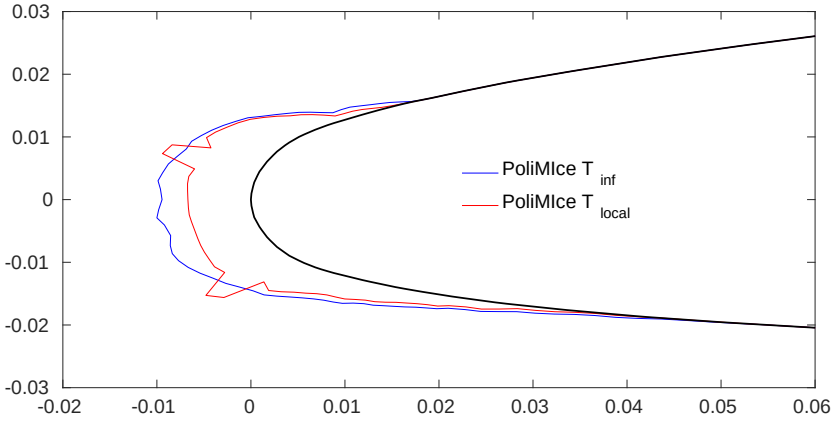

(c) PoliMIce

Fig. 12 Comparison of numerical results based on the free-stream temperature (blue lines) and the local temperature (red lines) for different icing models in mixed rime-glaze conditions (Tab. 7). Axes dimensions are in meters.

to substitute the constant, free-stream value considered in the Myers model. The temperature and mass flow corrections were found to produce significant improvement in the model accuracy with respect to Myers' one, with particular reference to atmospheric conditions where both glaze and rime accretion appear simultaneously on the body. Including the unsteady behavior of the temperature profile was not found to be very influential, possibly due to the low accretion rate of the considered cases.

References

[1] Gent, R. W., Dart, N. P., and Cansdale, J. T., "Aircraft icing," *Philosophical Transactions of The Royal Society A*, Vol. 358, No. 1776, 2000, pp. 2873–2911.

[2] Cebeci, T. and Kafyeke, F., "Aircraft Icing," *Annual Review of Fluid Mechanics*, Vol. 35, 2003, pp. 11–21.

[3] Lynch, F. T. and Khodadoust, A., "Effects of ice accretions on aircraft aerodynamics," *Progress in Aerospace Sciences*, Vol. 37, No. 8, 2001, pp. 669–767.

[4] Lou, D. and Hammond, D. W., "Heat and Mass Transfer for Ice Particle Ingestion Inside Aero-Engine," *Journal of Turbomachinery*, Vol. 133, No. 3, 2010, pp. 031021(1–5).

[5] Baars, W. J., Stearman, R. O., and Tinney, C. E., "A Review on the Impact of Icing on Aircraft Stability and Control," *Journal of Aeroelasticity and Structural Dynamics*, Vol. 2, No. 1, 2010, pp. 35–52.

[6] Makkonen, L., "Modeling power line icing in freezing precipitation," *Atmospheric Research*, Vol. 46, No. 1-2, 1998, pp. 131–142.

[7] Dalili, N., Edrisy, A., and Carriveau, R., "A review of surface engineering issues critical to wind turbine performance," *Renewable and Sustainable Energy Reviews*, Vol. 13, No. 2, 2009, pp. 428–438.

[8] Wright, W., "User's Manual for LEWICE Version 3.2," Contractor Report NASA/CR-2008-214255, NASA, 2008.

[9] Beaugendre, H., Morency, F., and Habashi, W. G., "FENSAP-ICEâĂŹs Three-Dimensional In-Flight Ice Accretion Module: ICE3D," *Journal of Aircraft*, Vol. 40, No. 2, 2003, pp. 239–247.

[10] Aliaga, C. N., Aubé, M. S., Baruzzi, G. S., and Habashi, W. G., "FENSAP-ICE-Unsteady: Unified In-Flight Icing Simulation Methodology for Aircraft, Rotorcraft, and Jet Engines," *Journal of Aircraft*, Vol. 48, No. 1, 2011, pp. 119–126.

[11] Myers, T. G. and Charpin, J. P. F., "A mathematical model for atmospheric ice accretion and water

low on a cold surface," *International Journal of Heat and Mass Transfer*, Vol. 47, 2004, pp. 5483–5500.

[12] Mingione, G. and Brandi, V., "Ice Accretion Prediction on Multielement Airfoils," *Journal of Aircraft*, Vol. 35, No. 2, 1998, pp. 240–246.

[13] Petrosino, F., Mingione, G., Carozza, A., Gilardoni, T., and D'Agostini, G., "Ice Accretion Model on Multi-Element Airfoil," *Journal of Aircraft*, Vol. 48, No. 6, 2011, pp. 1913–1920.

[14] Hedde, T. and Guffond, D., "ONERA Three-Dimensional Icing Model," *AIAA Journal*, Vol. 33, No. 6, 1995, pp. 1038–1045.

[15] Gori, G., Zocca, M., Garabelli, M., Guardone, A., and Quaranta, G., "PoliMIce: An Open Simulation Framework for Three-dimensional Ice Accretion," *Applied Mathematics and Computation*, Vol. 267, 2015, pp. 96–107.

[16] Messinger, B. L., "Equilibrium Temperature of an Unheated Icing Surface as a Function of Air Speed," *Journal of the Aeronautical Sciences*, Vol. 20, No. 1, 1953, pp. 29–42.

[17] Myers, T. G., "Extension to the Messinger Model fort Aircraft Icing," *AIAA Journal*, Vol. 39, No. 2, 2001, pp. 211–218.

[18] Politovich, K., "Predicting Glaze ore Rime Ice Growth on Airfoils," *Journal of Aircraft*, Vol. 37, No. 1, 2000, pp. 117–121.

[19] Borghi, E., Guardone, A., and Quaranta, G., "Assessment of an improved Myers model for airfoil icing," *3rd CEAS Air and Space Conference*, pp. 1733–1740.

[20] Stefan, J., "Ueber die theorie der eisbil-dung im polarmeere," *Annalen Der Physik Und Chemie*, Vol. 42, 1891, pp. 269–286.

[21] Caldwell, J. and Kwan, Y. Y., "Numerical methods for one-dimensional Stefan problems," *Communications in Numerical Methods in Engineering*, Vol. 20, 2004, pp. 535–545.

[22] Papadakis, M., Rachman, A., Wong, S. C., Hung, K. E., Vu, G. T., and Bidwell, C. S., "Experimental Study of Supercooled Large Droplet Impingement Effects," Technical Report DOT/FAA/AR-03/59, Federal Aviation Administration, 2003.

[23] "The OpenFOAM Foundation," http://www.openfoam.org/.

[24] Spalart, P. R. and Allmaras, S. R., "A One-Equation Turbulence Model for Aerodynamic Flows," *Recherche Aerospatiale*, Vol. 1, 1994, pp. 5–21.

[25] "NASA Langley Research Center Turbulence Modeling Resource," http://turbmodels.larc.nasa.gov/.

[26] Verdin, P., Charpin, J. P. F., and Thompson, C. P., "Multistep Results in ICECREMO2," *Journal of Aircraft*, Vol. 46, No. 5, 2009, pp. 1607–1613.

[27] Shepard, D., "A two-dimensional interpolation function for irregularly-spaced data," in "Proceedings of the 1968 ACM National Conference," ACM '68, 1968, pp. 517–524.

[28] W. B. Wright, D. G., R. W. Gent, "DRA/NASA/ONERA Collaboration on Icing Research Part II–Prediction of Airfoil Ice Accretion," NASA Contractor Report 202349, NASA, 1997.

[29] Jr., H. E. A., "Ice Accretions and Icing Effects for Modern Airfoils," Technical Publication NASA/TP-2000-210031, NASA, 2000.

[30] Anderson, D. N. and Tsao, J. C., "Additional Results of Ice-Accretion Scaling at SLD Conditions," NASA Contractor Report NASA/CRâĂŤ2005-213850, NASA, 2005.